We are IntechOpen, the world's leading publisher of Open Access books Built by scientists, for scientists

4,800
Open access books available

122,000
International authors and editors

135M
Downloads

Our authors are among the

154
Countries delivered to

TOP 1%
most cited scientists

12.2%
Contributors from top 500 universities

CLARIVATE ANALYTICS BOOK CITATION INDEX INDEXED

WEB OF SCIENCE™

Selection of our books indexed in the Book Citation Index in Web of Science™ Core Collection (BKCI)

Interested in publishing with us?
Contact book.department@intechopen.com

Numbers displayed above are based on latest data collected.
For more information visit www.intechopen.com

11

Multi-Wavelength and Multi-Direction Remote Sensing of Atmospheric Aerosols and Clouds

Hiroaki Kuze
Centre for Environmental Remote Sensing (CEReS), Chiba University
Japan

1. Introduction

Aerosols are liquid and solid particles floating in the atmosphere. Aerosol particles are originated from both natural and anthropogenic origins (Seinfeld & Pandis, 1998). In regard to the radiation balance of the Earth's atmosphere, aerosols reflect solar radiation back to space (direct effect), thus reducing the influence of greenhouse gases, though some type of aerosol causes opposite effects due to absorption of radiation. At the same time, aerosol particles work as nuclei for cloud condensation (indirect effect). Knowledge on these radiative effects of aerosol and cloud, however, is still insufficient so that uncertainties remain in the prediction of future global warming trends (IPCC, 2007). In this respect, intensive efforts are needed to evaluate the optical/physical properties of aerosols and clouds by means of both ground- and satellite-based remote sensing observations.

In order to obtain better understanding of these particulate matters, what is obviously needed is the monitoring technique that enables the retrieval of their optical properties. In this chapter, we propose multi-wavelength and multi-directional remote sensing of atmospheric aerosols and clouds. The proposed method consists of the application of ground-based radiation measurement, lidar measurement, differential optical absorption spectroscopy (DOAS), and satellite observations using natural as well as artificial light sources. Such combinatory approach makes it possible to measure various aspects of radiation transfer through the atmosphere, especially the influence of tropospheric aerosols and clouds. Also, the data provided from the ground-based solar irradiance/sky radiance measurement and DOAS are valuable for precisely characterizing the optical property of aerosol particles near the ground level, including the information from both particulate scattering and gaseous absorption. Such ground data are also indispensable for the atmospheric correction of satellite remote sensing data in and around the visible range of the radiation spectrum. The multi-wavelength and multi-directional observation schemes treated in the present chapter are summarized in Table 1.

2. Differential optical absorption spectroscopy (DOAS)

The method of differential optical absorption spectroscopy (DOAS) provides a useful tool for monitoring atmospheric pollutants through the measurement of optical extinction (i.e., the sum of absorption and scattering) over a light path length of a few kilometres (Yoshii et al., 2003, Lee et al., 2009; Si et al., 2005; Kuriyama et al., 2011). The DOAS method in the

Scheme	Wavelength	Direction	Aerosol	Trace gas
DOAS	UV, VIS, and NIR, with the resolution of array detector	Nearly horizontal measurement	Measurable through the spectral intensity	Measurable (e.g. NO_2 around 450 nm)
solar/skylight	UV and VIS, with the resolution of array detector	Solar direction/ any direction including the zenith	Measurable through the spectral intensity	Measurable (e.g. H_2O around 720 nm)
Lidar	Fundamental and harmonics of Nd:YAG laser (1064, 532 and 355 nm)	Vertical and slant path observations	Profiling by solving the lidar equation	Not applicable unless tunable lasers are employed
Satellite	Spectral bands in UV, VIS, and NIR	Nadir or near-nadir directions	Evaluated and removed in the process of atmospheric correction	Spectral bands are usually too wide to retrieve trace gases

Table 1. Various schemes of atmospheric observation discussed in this chapter.

visible spectral region is quite suitable for urban air pollution studies, since both nitrogen dioxide (NO_2) and aerosol, the most important pollutants originated from human activities, can directly be measured using a near horizontal light path in the lower troposphere.

Although conventional approach in the DOAS measurement is to install a light source, our group at the Centre for Environmental Remote Sensing (CEReS), Chiba University, has established a unique DOAS approach based on aviation obstruction lights (white flashlights) equipped at tall constructions such as smokestacks (Yoshii et al., 2003, Si et al., 2005; Kuriyama et al., 2011). Since those xenon lamps produce flash pulses every 1.5 s during the daytime, they can easily be recognized with the coverage of the whole visible spectral range. Thus, a simple setup consisting of an astronomical telescope and a compact spectro-radiometer can be employed for the measurement of NO_2. Also, the stable intensity of the light source makes it possible to retrieve aerosol, or suspended particulate matter (SPM) concentration in the lower troposphere, since the intensity variation of the detected light is mostly ascribable to the aerosol extinction over the light path (Yoshii et al., 2003).

As shown in Figs. 1 and 2, the principle of DOAS analysis of NO_2 concentration is based on matching high-pass filtered spectral (wavelength) features between the DOAS-observed optical thickness ($\Delta\tau$) and laboratory-observed molecular absorption spectrum ($\Delta\sigma$). Because of the Lambert-Beer's law, the optical thickness, τ, is expressed as

$$\tau = -\ln(I / I_0), \tag{1}$$

where I and I_0 stand for the observed and reference spectrum, respectively. The reference spectrum can be obtained by either operating the DOAS spectrometer at a short distance

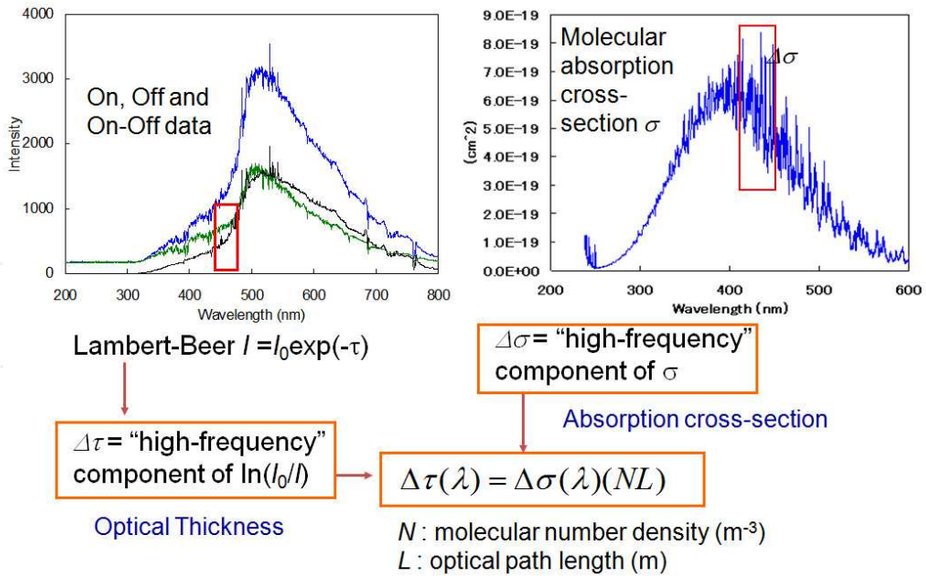

Fig. 1. Schematic flow of the DOAS analysis. The net radiation from the pulsed light source can be retrieved by subtracting the background due to sky radiation, and an appropriate portion of the spectrum is compared with the molecular cross-section spectrum obtained from laboratory measurement. Then, the "high-frequency" components of the observed optical thickness (Δτ) and cross-section data (Δσ) are compared to derive the molecular number density along the optical path length, *L*.

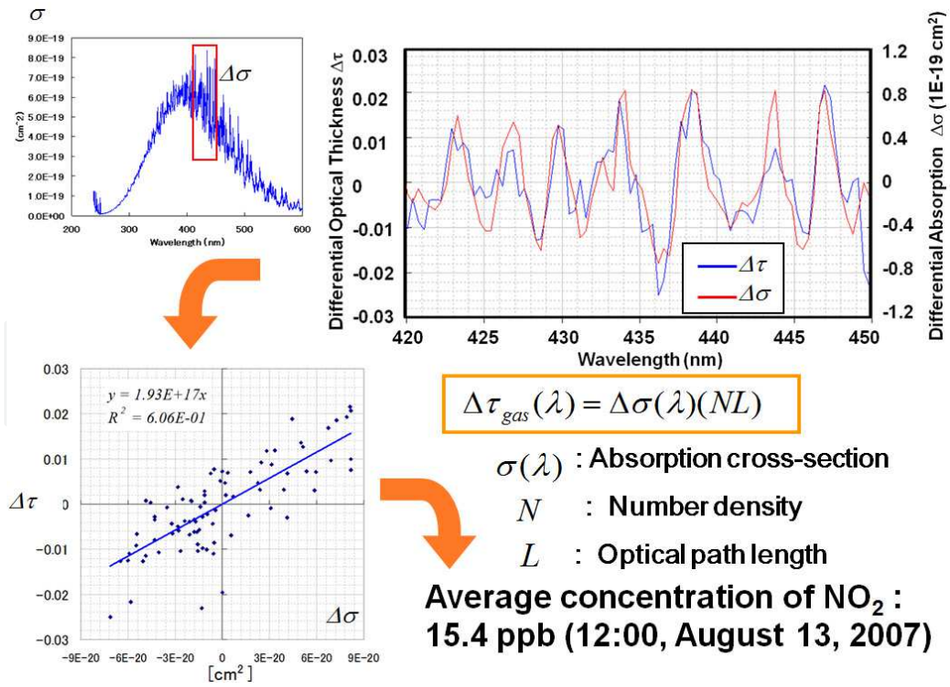

Fig. 2. An example of DOAS spectral matching, in which the correlation between the differential optical thickness from the DOAS data and differential absorption is examined to determine the average volume concentration of NO_2 molecules.

from the light source, or observing the spectrum under very clear atmospheric conditions with minimal aerosol loading. The optical thickness is generally proportional to the product of extinction coefficient, α, and the light path length, L, i.e., $\tau = \alpha L$. In the case of molecular absorption, the extinction coefficient is equal to the absorption coefficient, which can be given as the product of absorption cross-section, σ, and the molecular number density, N, i.e., $\alpha = N\sigma$. Although molecular scattering (Rayleigh scattering) and aerosol scattering (Mie scattering) also exist, their contribution can be eliminated by applying the high-pass filtering to both τ (λ) and σ (λ) (where λ is wavelength), since the absorption feature of NO_2 is a rapidly varying function with wavelength (see insets in Figs. 1 and 2), while the wavelength dependence of Rayleigh or Mie scattering is much more moderate. Thus, after the high-pass filtering, one obtains

$$\Delta\tau = (NL)\Delta\sigma. \tag{2}$$

This indicates that the correlation analysis between the rapidly varying components of the optical thickness and NO_2 cross-section in an appropriate wavelength range can lead to the determination of the molecular number density, hence the volume concentration ratio, of NO_2 along the DOAS observation light path. An example of the retrieval of NO_2 in the Chiba city area is shown in Fig. 3. In this case, the DOAS result shows the average concentration over a light path length of 5.5 km. From Fig. 3, it is seen that the DOAS data show good temporal correlation with the ground sampling data from nearby sampling stations. Note that the temporal resolution (5 min) of the DOAS observation is much better than that of the ground sampling (1 h). The observation of DOAS spectra is limited to daytime, since the white flashlight (Xe light) is replaced with blinking red lamps during night time.

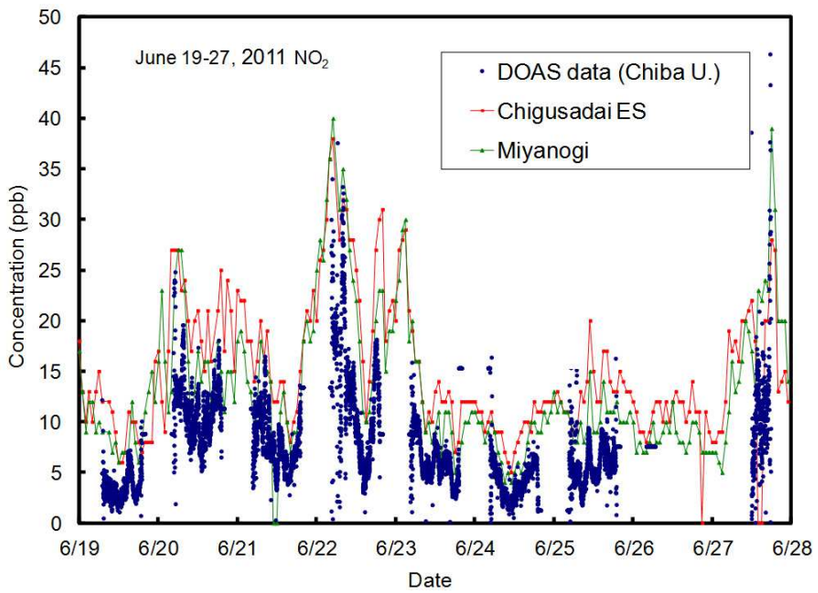

Fig. 3. Comparison of NO_2 volume concentration between the DOAS and conventional ground sampling measurements during June 19 - 27, 2011. The DOAS data are based on the measurement at CEReS, Chiba University, using an aviation obstruction flashlamp located around 5.5 km in the north direction. The ground sampling data are from two nearby sampling stations (Chigusadai Elementary School and Miyanogi stations) operated by the municipal government.

The analysis of light intensity detected with a DOAS spectrometer can yield information also on aerosol extinction along the light path. The wavelength dependence of each atmospheric component is exemplified in Fig. 4(a), where it is apparent that the contribution from aerosol extinction is much more significant than that from either NO_2 or molecular Rayleigh scattering. The optical thickness associated with aerosol extinction can generally be given as

$$\tau(\lambda) = B(\lambda / \lambda_0)^{-A}, \tag{3}$$

where $A=\alpha_{ang}$ is called the Angstrom exponent and B the turbidity constant. The value of A changes with the aerosol size distribution in such a way that a smaller value (~ 0.5) indicate the dominance of relatively coarse particles (such as sea salt or dust), while a large value (~ 2) that of relatively fine particles (such as ammonium sulfate or ammonium nitrate). The value of B, on the other hand, is equal to the aerosol optical thickness as wavelength λ_0,

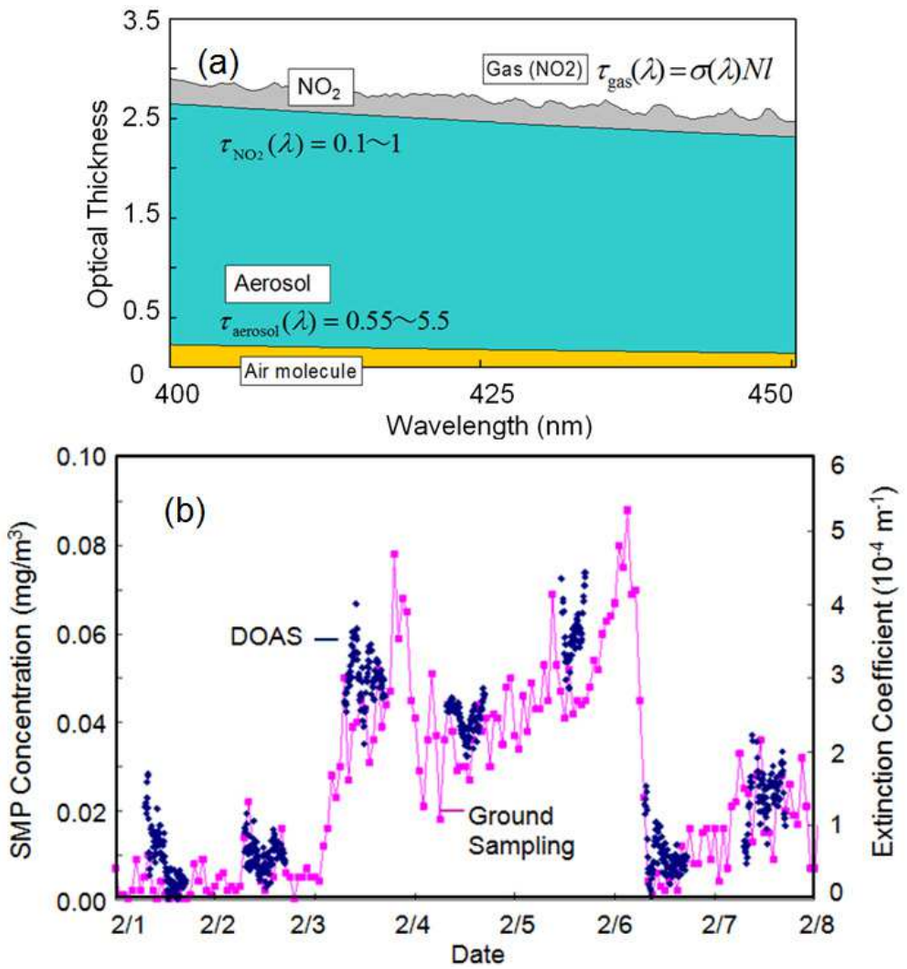

Fig. 4. Aerosol measurement from DOAS data: (a) comparison of contributions of gas (NO_2) absorption, aerosol extinction, and molecular extinction (Rayleigh scattering) to DOAS optical thickness, and (b) temporal change of SPM concentration from ground sampling and aerosol extinction coefficient from DOAS during February 1 to 7, 2011 observed in Chiba.

which is chosen to be 550 nm or some appropriate value within the observation wavelength range. Figure 4(b) shows the result of analysis based on eq. (4). As seen from Fig. 4(b) the temporal variation shows good agreement between the DOAS-derived aerosol optical thickness and the SPM mass concentration observed from the ground sampling.

3. Solar and skylight radiation measurement

For aerosols, network observation activities have been undertaken in terms of skyradiometer measurements (Takamura & Nakajima, 2004). Alternatively, the use of a compact, stand-alone spectroradiometer (EKO, MS-720) enables the spectral measurements of direct solar radiation (DSR), solar aureole (AUR) and scattered solar radiation (SSR) (Manago & Kuze, 2010; Manago et al., 2010). Since the instrument is powered by batteries with no PC requirement during measurements, it provides better portability compared to a skyradiometer. The wavelength coverage between 350 and 1050 nm with a resolution of 10 nm is useful for precise evaluation of the aerosol optical properties as well as that of the water vapor column amount. The wide dynamic-range measurement of both the direct and scattered solar radiation is attained by means of a thick diffuser and a stable photodiode array, in combination with the automatic exposure control equipped to the handy spectroradiometer (MS-720) (Manago & Kuze, 2011). In order to facilitate the radiation transfer calculation in the retrieval procedure, home-made baffle tubes are used to limit the field of view (FOV) of the observation to 20 deg (SSR) and 5 deg (DSR).

The radiation measurements were conducted at the CEReS site (35.62^{o}N, 140.10^{o}E) under clear-sky conditions, mostly around noon. The SSR measurements were made in 24 directions (north, east, south, and west directions, each with 6 elevation angles). The DSR and AUR components were measured before and after the SSR measurements. The total time required for a set of DSR, AUR, and SSR data was 30 - 40 minutes. Approximately 130 datasets were obtained during the observation period from August 2007 to March 2009.

Independent measurement of AOD was carried out with a sunphotometer (Prede, PSF-100). This instrument has four channels centred at 368, 500, 675, and 778 nm, each having the bandwidth of 5 nm. The wavelength dependence of AOT is analyzed with eq. (3) to obtain the Angstrom exponent. During the daytime the AOD is retrieved from the solar radiation intensity within a FOV of 1 deg at an interval of 10 s. From the sunphotometer measurement, $A=\alpha_{ang}$ and the coefficient B (turbidity constant at the reference wavelength λ_0= 550 nm in this case) can be retrieved.

In our ground observation with the battery-operated spectroradiometer, the direct solar irradiance, aureole radiance, and scattered solar radiance were measured in various directions as mentioned above. Even with these detailed measurements, however, usually it is not possible to determine the complete composition of aerosol particles. Thus, we rely on the three-component aerosol model (TCAM), in which three aerosol types of water soluble, oceanic, and soot components are considered as a basis set which is “quasi-complete” to describe the aerosol optical parameters, namely the wavelength dependence of extinction coefficient, single scattering albedo, asymmetry parameter, and scattering phase function. Figure 5 shows the wavelength dependence of the real and imaginary parts of the aerosol refractive index for the three aerosol components. It has been shown that most of the irradiance/radiance values are well reproduced by appropriately adjusting the total and

relative contributions of these three basis components as well as the size distribution of each component (Manago et al, 2011). As seen from Fig. 5, the soot component shows remarkably high value of the imaginary part of the refractive index. This indicates that the absorption property is higher (single scattering albedo is lower) for aerosol with more contribution of soot particles. Figure 6 shows an example of the results of the irradiance and radiance observations. Figure 7 shows an example of aerosol optical parameters derived from the TCAM analysis of the data: Fig. 7(a) shows the wavelength dependence of the aerosol extinction coefficient (normalized to the value at 550 nm), (b) single scattering albedo, (c) asymmetry parameter, and (d) scattering phase function at wavelength 550 nm. In Sec. 5 below, we describe the application of these aerosol characteristics to the atmospheric correction of satellite remote sensing data.

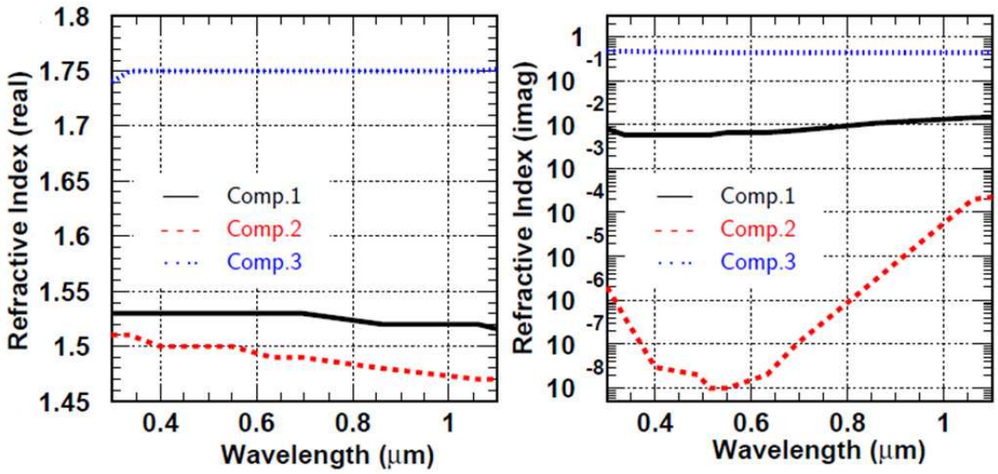

Fig. 5. Real and imaginary parts of the complex refractive index of the three aerosol components: component 1, 2 and 3 refer to the water soluble, oceanic, and soot aerosol types, respectively.

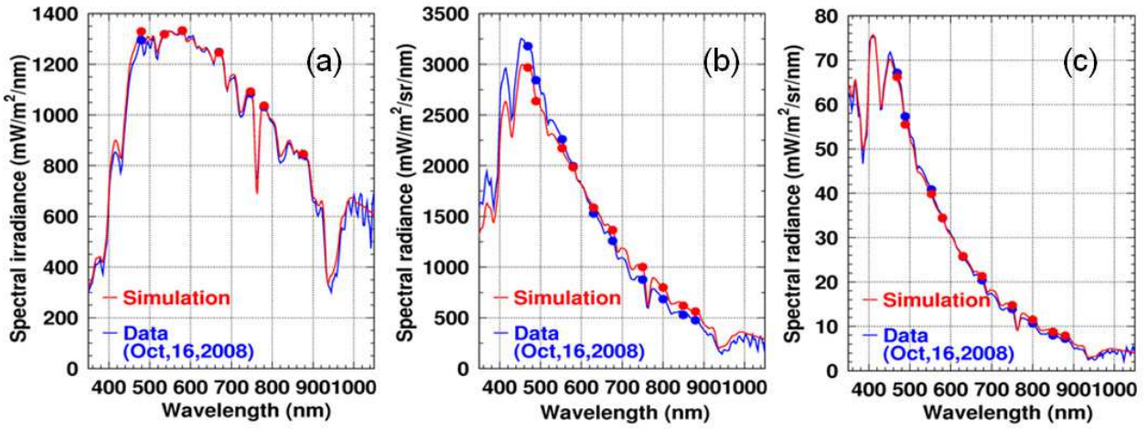

Fig. 6. Spectra observed around noon on October 16, 2008: (a) direct solar radiation (DSR), (b) aureole (AUR), and (c) scattered solar radiation (SSR). Acceptance angle of the instrument is 5 deg for DSR, 5-20 deg for AUR, and 20 deg for SSR. Simulation curves based on the TCAM best fitting are also shown with data points (circles) used for the fitting.

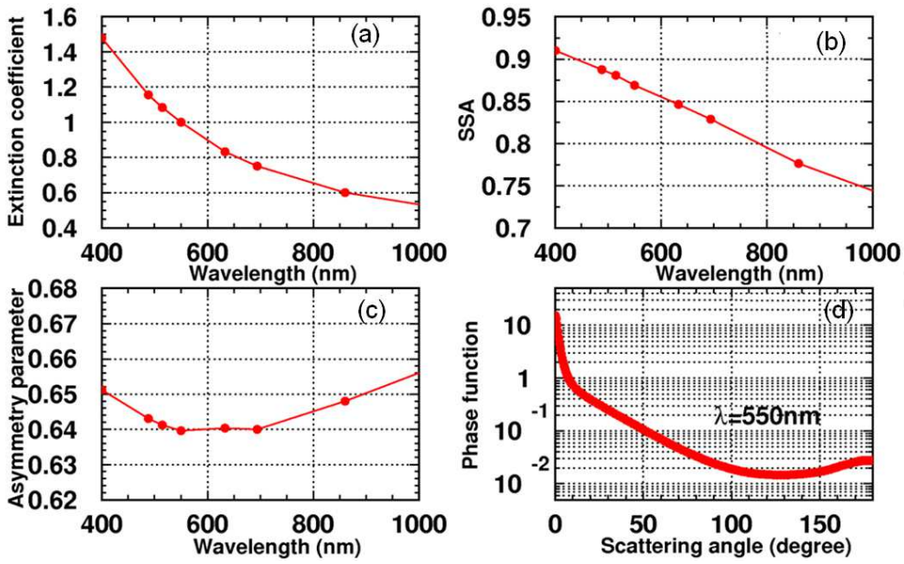

Fig. 7. Aerosol optical parameters derived from the TCAM analysis of the data shown in Fig. 6: (a) wavelength dependence of the aerosol extinction coefficient (normalized to the value at 550 nm), (b) single scattering albedo, (c) asymmetry parameter, and (d) scattering phase function at wavelength 550 nm.

4. Lidar measurement of aerosols and clouds

While the DOAS method and skylight/solar radiation measurement lead to the retrieval of atmospheric information integrated over optical paths, the lidar measurement makes it possible to measure aerosol and cloud distributions (profiles) along the optical path. Here we report the result of multi-wavelength lidar measurement conducted at CEReS. Conventionally lidar data have been analyzed by means of the Fernald method (Fernald, 1984), in which the lidar equation

$$P(R) = P_0 \frac{c\tau}{2} AK \frac{G(R)}{R^2} \beta(R) \exp\left[-2\int_0^R \alpha(R')\, dR'\right] \tag{4}$$

is solved by starting the integration from the far-end boundary. In eq. (4), $P(R)$ is the power detected by the lidar system corresponding to a distance R, P_0 is the power of the emitted laser radiation, c is the speed of light, τ is the time duration of the laser pulse, A is the area of the lidar telescope, $G(R)$ is the function describing the overlap between the laser beam and telescope field of view, $\beta(R)$ is the backscattering coefficient, and $\alpha(R)$ is the extinction coefficient. Since both air molecules and aerosol particles contribute to the scattering and extinction, one needs to separate these two components in solving the lidar equation. This can be achieved by introducing the ratio between the extinction coefficient and the backscattering coefficient. Thus, for aerosols,

$$S_1(R) = \alpha_1(R) / \beta_1(R) = \sigma_1(R) / \left(\frac{d\sigma_1}{d\Omega}\right)_{\theta=\pi} \tag{5}$$

is assumed, whereas for air molecules,

$$S_2 = \alpha_2(R) / \beta_2(R) = 8.52 \ \text{(sr)} \tag{6}$$

is used as a constant. In eqs. (5) and (6), suffix 1 and 2 refer to aerosol and air molecule, respectively. In eq. (5), $\sigma_1(R)$ and $(d\sigma_1/d\Omega)_{\theta=\pi}$ indicate the total cross-section and backward differential cross-section of aerosol scattering, respectively. The parameter S_1 is often called the lidar ratio. In eq. (6), the range dependence of S_2 is omitted, since the composition of air molecules is stable througout the troposphere. Under these assumptions, the lidar equation can be analytically solved as

$$\alpha_1(R) = -\frac{S_1(R)}{S_2}\alpha_2(R) + \frac{S_1(R)\, X(R) \exp I(R)}{\dfrac{X(R_c)}{\dfrac{\alpha_1(R_c)}{S_1(R_c)} + \dfrac{\alpha_2(R_c)}{S_2}} + J(R)}. \tag{7}$$

Here

$$X(R) = R^2 P(R) \tag{8}$$

is the range-corrected signal, and functions $I(R)$ and $J(R)$ are defined as

$$I(R) = 2\int_R^{R_c} \left[\frac{S_1(R')}{S_2} - 1\right] \alpha_2(R')\, \mathrm{d}R' \tag{9}$$

and

$$J(R) = 2\int_R^{R_c} S_1(R')\, X(R') \exp I(R')\, \mathrm{d}R'. \tag{10}$$

In eqs. (7), (9) and (10), R_c denotes the range of a far-end boundary, at which each integration is started. The reason that a far-end boundary value is assumed rather than a near-end boundary value is the stability of the numerical evaluation of eq. (7) (Fernald 1984).

Usually signals of a vertically looking lider are analyzed assuming that the aerosol property does not change with the altitude. Under this assumption, the range dependence in eq. (5) can be neglected. Even in this case, however, it is necessary to determine the value of lidar ratio as a function of wavelength [$S_1=S_1(\lambda)$] in order to analyze multi- wavenength lidar data. One way to accomplish this is to use ancillary data from a sunphotometer (Kinjo et al., 1999), since the wavelength dependence of optical thickness provides a constraint to the intagration of $\alpha_1(R, \lambda)$ from R=0 to $R = R_c$. Another approach is to employ the aerosol properties measured at the ground level. In the case of Fig. 8, for example, the S_1 values of 54.7, 53.0, 46.0 and 43.2 sr are used for λ = 355, 532, 756 and 1064 nm, respectively, as derived from the chemical analysis of ground sampling data taken monthly at CEReS (Fukagawa et al., 2006). In Fig. 8, panel (a) shows the temporal variation of the aerosol extinction profile measured for 1064 nm and relative humidity (RH) at the ground level, while panel (b) depicts that of the profile of the Angstrom exponent, α_{ang}, as derived from the analysis of lidar data for the four wavelengths. The features in these panels indicate

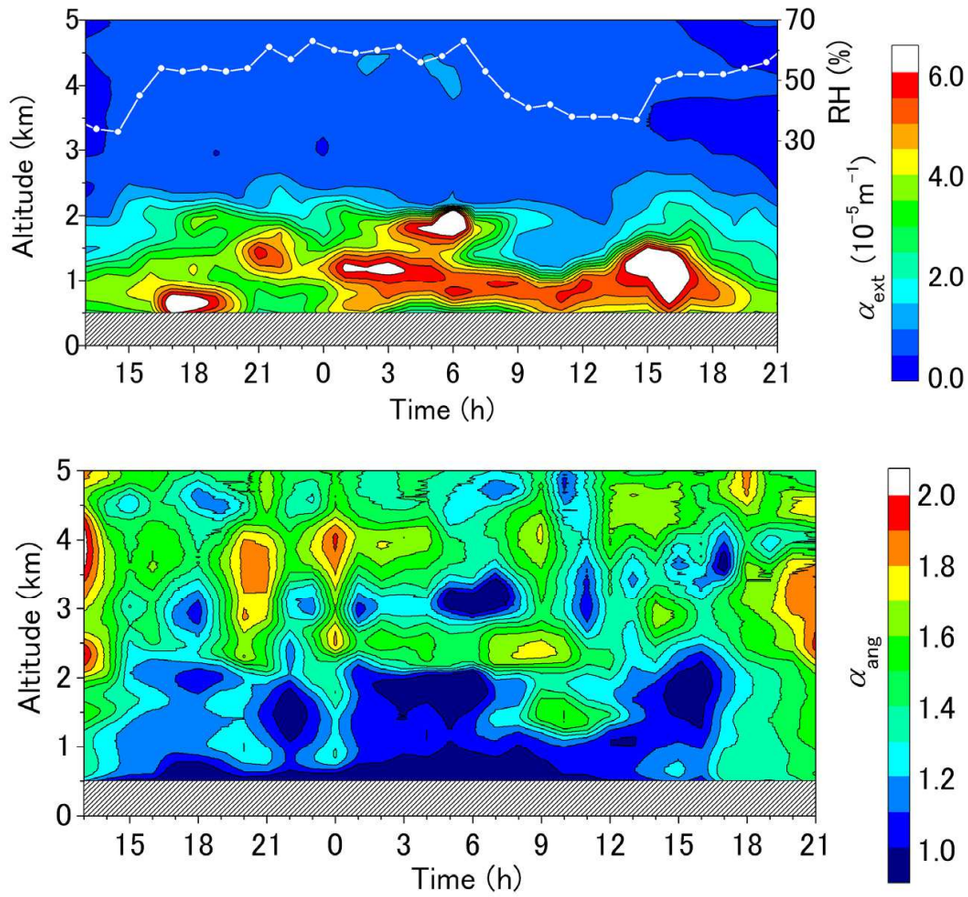

Fig. 8. Analysis of vertical looking multi-wavelength lidar data: (a) extinction profile for wavelength λ = 1064 nm observed at CEReS on 17-18 November 2005, and Angstrom exponent derived from extinction coefficients observed for λ = 355, 532, 756 and 1064 nm. The analysis is based on the Fernald method with lidar parameters S_1 = 54.7, 53.0, 46.0 and 43.2 sr for each lidar wavelength (based on sampling result at CEReS) and the reference altitude of R_c = 5.5 km.

that relatively higher extinction near the ground level is observed when RH increases, and at the same time, smaller values of α_{ang} are observed. It is likely that both of these observations are due to the aerosol growth associated with the increase of RH.

5. Atmospheric correction of satellite remote sensing data

Images taken from satellite sensors are affected by both the ground reflectance and atmospheric conditions, which include the influence of scattering and absorption of air molecules and aerosol particles. The process of atmospheric correction, in which such atmospheric effects are precisely evaluated and removed, is indispensable for extracting the intrinsic information of the ground reflectance from satellite imagery (Tang et al., 2005; Kaufman et al., 1997). Although it is rather straightforward to make corrections on the Rayleigh scattering of air molecules, aerosol particles are quite variable both temporally and spatially. This is due to the variable origins of aerosols, consisting of relatively coarse

particles of natural origins (such as sea-salt and soil particles) and relatively fine particles of anthropogenic origins (such as sulphate and soot particles).

In standard atmospheric correction, it is customary to assume some representative aerosol models such as maritime, rural, continental, or urban aerosol, to implement the radiative transfer calculation of a satellite scene. This approach has an obvious disadvantage that if the assumed aerosol properties are different from those of real aerosols included in the satellite scene, the resulting information on the ground reflectance is inaccurate. To overcome this difficulty, here we use the aerosol information derived from the ground observation implemented nearly simultaneously with the satellite overpass. Such ancillary information ensures better separation of the ground and atmospheric effects from satellite imagery. Figure 9 shows the schematic drawing of radiation components considered in the radiative transfer calculation (Kotchenova et al., 2006). In this scheme, the radiance originated from the target area is denoted as L_{tar}, which consists of the ground direct (L_{gd}) and ground indirect (L_{gi} and L_{gi}') components. The environmental radiance, L_{env}, is the component associated with the surface reflection that takes place in adjacent pixels. The atmospheric radiance, L_{atm}, consists of two terms, namely, the path radiance due to single scattering (L_{ps}) and that due to multiple scattering (L_{pm}).

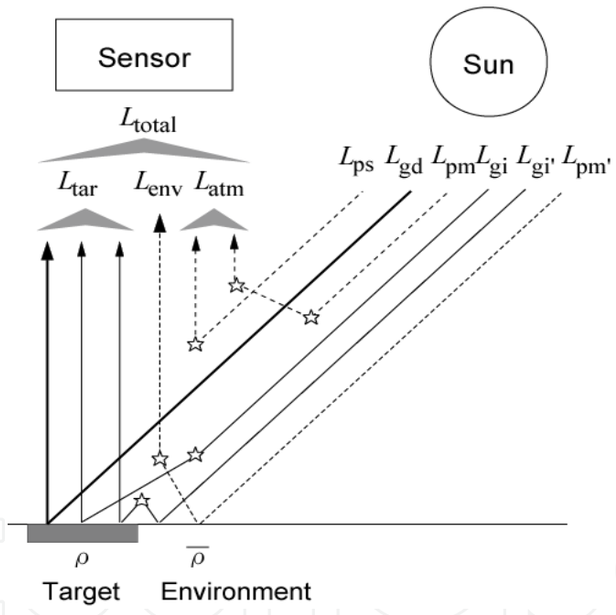

Fig. 9. Schematic drawing of radiation components considered in the radiative transfer calculation. See text for the explanation of radiance components shown in this figure.

In the present research, the ground measurement by means of a compact spectroradiometer was implemented in synchronous with the overpass of the satellite observation. The aerosol optical parameters were derived by analyzing both the direct solar radiation (DSR) and scattered solar radiation (SSR) through the Mie-scattering and radiative transfer calculations, as explained in Sec. 3 of this chapter. When the aerosol loading is relatively small (clear days), it is likely that the aerosol model resulting from this procedure can be applicable to the whole region of the Moderate Resolution Imaging Spectroradiometer (MODIS) image, and the atmospheric correction is applied to the image. Since this correction

is based on the aerosol model from the simultaneous measurement, the resulting distribution of the surface reflectance is considered to be more reliable than the result that would be obtained by assuming usually available "standard" aerosol models such as urban, rural, or oceanic models. The surface reflectance map (ρ_{clear} map) on such a "clear" day, in turn, can be used as a standard for that particular season of the year, and the atmospheric correction of MODIS data taken on more turbid days can be implemented on the basis of these standard ρ_{clear} maps. This process leads to the derivation of the distribution of aerosol optical thickness (τ map).

For each of the visible bands of MODIS, a lookup table of the radiance at the top of the atmosphere, $L_{total}(\rho, \tau_{550})$, was constructed on the basis of the aerosol optical parameters and the geometric data describing the observational conditions of each image. Here, ρ is the diffuse reflectance of each pixel, and τ_{550} is the aerosol optical thickness (AOT) at wavelength 550 nm. The reflectance property of the surface was assumed to be Lambertian, and the radiative transfer calculation was carried out using the 6S code (Kotchenova et al., 2006).

The atmospheric correction was applied to channels 1 through 4 covering wavelength range between 0.450 and 0.876 μm of the Terra/MODIS and Aqua/MODIS images. The ground resolution of the MODIS sensor is 0.5 km×0.5 km/pixel. The region of 600×600 pixels around Chiba University was extracted from each of the MODIS images, which were taken from the satellite data archiving system of CEReS, Chiba University. The ground observations using the spectroradiometer were carried out at CEReS around noon on nearly cloud-free days from 2007 to 2009 (around 130 days). In order to take the time lag of around 2 h between the satellite overpass (10:00 local time) and the spectroradiometer observation (12:00) into account, the sunphotometer data taken at CEReS were employed to examine the temporal stability of atmospheric conditions. If the AOT derived from the spectroradiometer was close to the AOT value measured with the sunphotometer at the time of satellite overpass, the data were employed in the atmospheric correction. Otherwise, the data were not included in the clear-day analysis lest the instability in the atmospheric condition might also degrade the regional stability (i.e. homogeneity) of the aerosol distribution. Figure 10 shows the wavelength dependence of the surface reflectance (ρ_{clear} map) of the pixel including the location of Chiba University for various months in the year 2008.

Figure 11 shows the seasonal variation of the surface reflectance for the Chiba University pixel obtained from the analysis of MODIS band 4 centred at 550 nm. For the sake of comparison, our previous result obtained from the Landsat-5 analysis is also depicted (Todate et al., 2004). Note that the Landsat reflectance was obtained assuming a standard aerosol model (maritime), whereas the TCAM aerosol model is used in the present MODIS analysis. Pixels with vegetation and soil coverage are shown for the Landsat data, since the ground resolution associated with this sensor (30 m) is much better than the MODIS resolution of 500 m. From Fig. 11, it is seen that the surface reflectance decreases from November to December, due to the decrease in the vegetation coverage during winter. In winter the reflectance shows no critical dependence on the aerosol model assumed in the atmospheric correction because of the fact that the AOT tends to be small. In summer, on the contrary, the AOT generally increases so that the resulting value of surface reflectance varies in accordance with the aerosol model employed in the analysis.

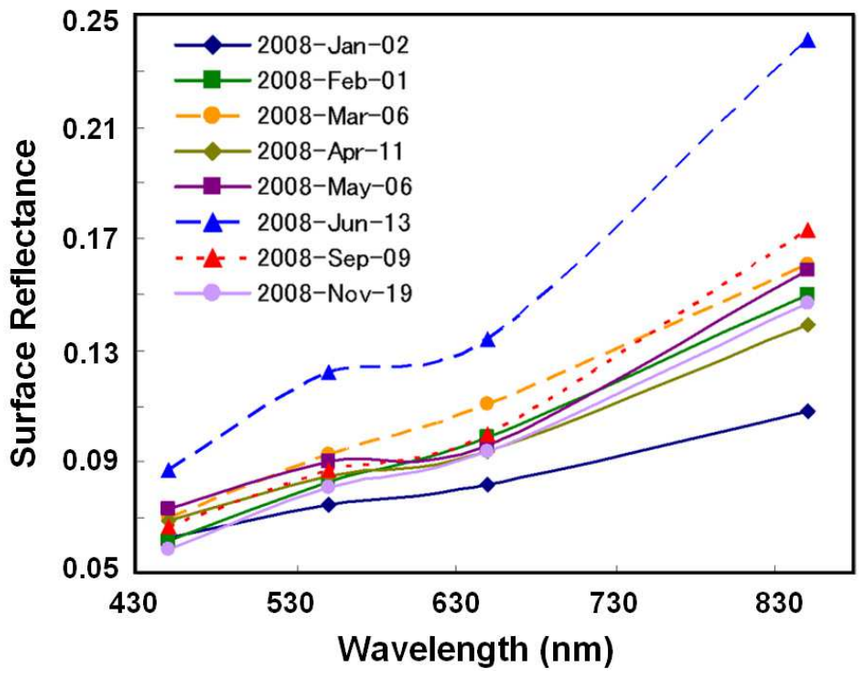

Fig. 10. Surface reflectance at Chiba University (2008)

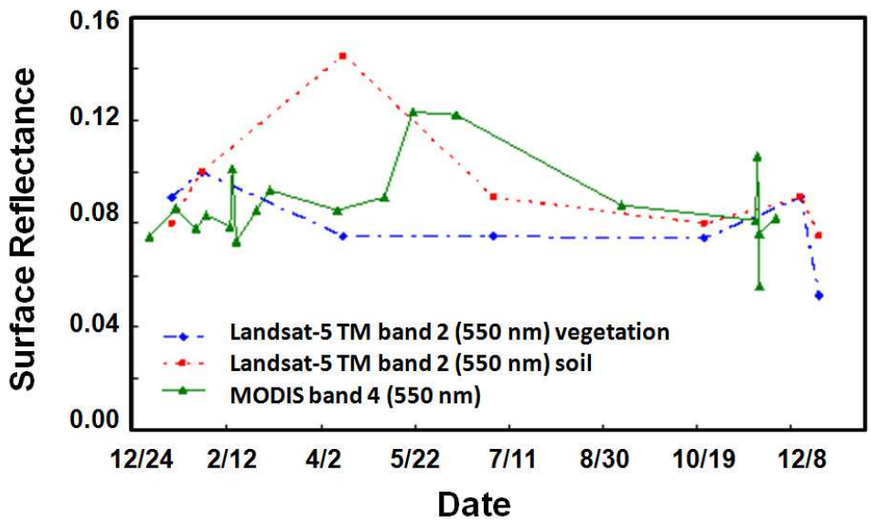

Fig. 11. Seasonal variation of surface reflectance at the MODIS pixel including the Chiba university campus (λ =550 nm).

From the present TCAM analysis of MODIS data, monthly reflectance image ($\rho_{monthly}$) is generated for each month as a composite of pixels that exhibit the lowest reflectance. This process ensures the removal of cloud pixels that might contaminate the resulting ρ map. These monthly ρ maps, in turn, are employed in the radiative transfer analysis to derive the aerosol distribution (τ map) from images taken on relatively turbid days. Examples of the reflectance and aerosol distribution images are shown in Fig. 12.

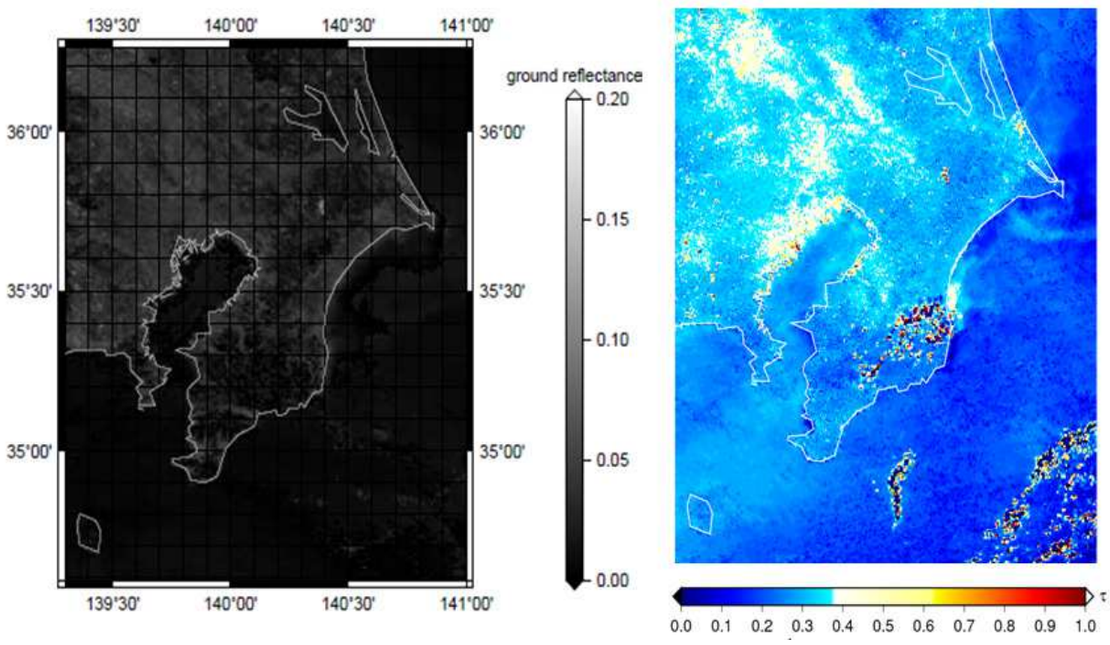

Fig. 12. Analysis of MODIS data in November 2007: (a) surface reflectance map (540 - 570 nm), and (b) aerosol optical thickness at 550 nm on 24 November 2007.

6. Conclusion

Optical properties of aerosols and clouds play an important role in the consideration of the Earth's radiation budget. In this chapter, we have described multi-wavelength and multi-directional remote sensing of the troposphere, putting emphasis on the visible part of the spectrum. The DOAS approach enables the direct observation of air pollutants by employing a nearly horizontal light path in the lowest part of troposphere, where the highest concentrations of pollutants such as NO_2 and aerosol (SPM) are found. The observation of direct solar radiation and scattered solar radiation (sky light), on the other hand, is useful for retrieving detailed aerosol optical properties under clear-sky conditions. Thus, the data can be quite useful for implementing precise atmospheric correction on satellite-observed imagery that includes the ground observation point. The multi-wavelength lidar observation provides an efficient tool to elucidate the vertical profiles of aerosol particles. By combining the lidar data with some appropriate ancillary data such as the ground-level characterization of aerosol properties, it becomes possible to derive useful information on temporal as well as spatial information on aerosol and cloud characteristics in the atmosphere.

7. Acknowledgment

We acknowledge the financial support of the Grant-in-Aid from the Ministry of Education, Culture, Sports, Science & Technology in Japan (#21510006). Also, contributions of a number of graduate students who participated in various researches presented in this chapter are gratefully acknowledged.

8. References

Fernald, F. G., Analysis of atmospheric lidar observation: some comments. Appl. Opt. Vol 23, (1984), pp. 652-653, ISSN 0003-6935

Fukagawa, S., Kuze, H., Bagtasa, G., Naito, S., Yabuki, M., Takamura, T., Takeuchi, N., Characterization of seasonal and long-term variation of tropospheric aerosols in Chiba, Japan. Atmospheric Environment, Vol. 40, No.12, (2006), pp. 2160-2169, ISSN 1352-2310

Intergovernmental Panel on Climate Change (IPCC), *Climate Change 2007: The Physical Science Basis*, Cambridge Univ. Press (2007) ISBN-13: 978-0521705967, Cambridge, U.K.

Kaufman, Y. J., Tanré, D., Gordon, H. R., Nakajima, T., Lenoble, J., Frouins, R., Grassl, H.,Herman, B. M., King, M. D., Teillet, P. M., Passive remote sensing of tropospheric aerosol and atmospheric correction for the aerosol effect. J. Geophys. Res., Vol.102, No.D14, (1997), pp. 16,815-16,830, ISSN 0148-0227

Kinjo, H., Kuze, H., Takeuchi, N., Calibration of the Lidar Measurement of Tropospheric Aerosol Extinction Coefficients. Jpn. J. Appl. Phys. Vol. 38, (1999), pp. 293-297, ISSN 0021-4922

Kotchenova, S.Y., Vermote, E.F., Matarrese, R., Klemm, Jr. F.J., Validation of a vector version of the 6S radiative transfer code for atmospheric correction of satellite data. Part I: Path radiance. Applied Optics Vol. 45, No. 26, No.10 (September 2006), pp.6762-6774, ISSN 0003-6935

Kuriyama, K., Kaba, Y., Yoshii, Y., Miyazawa, S., Manago, N., Harada, I., Kuze, H., Pulsed differential optical absorption spectroscopy applied to air pollution measurement in urban troposphere. J. Quantitative Spectroscopy & Radiative Transfer, Vol. 112, (2011), pp. 277-284, ISSN 0022-4073

Lee, H.; Kim, Y.J., Jung, J., Lee, C., Heue, K.P., Platt, U., Hu, M., 6 Zhu, T., Spatial and temporal variations in NO_2 distributions over Beijing, China measured by imaging differential optical absorption spectroscopy. J. Environ. Management, Vol. 90, No.5, (April 2009), pp. 1814-1823, ISSN 0301-4797

Manago, N., Kuze, H., Determination of tropospheric aerosol characteristics by spectral measurements of solar radiation using a compact, stand-alone spectroradiometer. Appl. Opt. Vol. 49, (2010), pp. 1446-1458, ISSN 1539-4522

Manago, N., Miyazawa, S., Bannu, Kuze, H., Seasonal variation of tropospheric aerosol properties by direct and scattered solar radiation spectroscopy. J. Quantitative Spectroscopy & Radiative Transfer, Vol. 112, Issue 2, (January 2011), pp. 285-291, ISSN 0022-4073

Miyazawa, S., Manago, N., Kuze, H., Precice atmospheric correction of MODIS data using aerosol optical parameters derived from simultaneous ground measurement, in Proceedings of the 49th Annual Meeting of the Remote Sensing Society of Japan, (2010), pp.245-246 (*in Japanese*)

Seinfeld, H. and Pandis, S.N. (1998). *Atmospheric Chemistry and Physics, from Air Pollution to Climate Change*, John Wiley, ISBN 0-471-17815-2, New York, U.S.A.

Si, F., Kuze, H., Yoshii, Y., Nemoto, M., Takeuchi, N., Kimura, T., Umekawa, T., Yoshida, T., Hioki, T., Tsutsui, T., Kawasaki, M., Measurement of regional distribution of atmospheric NO_2 and aerosol particles with flashlight long-path optical monitoring. Atmos. Environ. Vol. 39, (2005), pp. 4959-4968, ISSN 1352-2310

Takamura, T., Nakajima, T., Overview of SKYNET and its activities. Optica Pura y Aplicada Vol. 37, (2004), pp. 3303–3308, ISSN 0030-3917

Tang, J., Xue, Y., Yu, T., Guan,Y. Aerosol optical thickness determination by exploiting the synergy of TERRA and AQUA MODIS. Remote Sensing of Environment Vol. 94, (2005), pp. 327–334, ISSN 0034-4257

Todate, Y., Minomura, M., Kuze, H., Takeuchi, N., On the retrieval of aerosol information on the land surface from Landsat-5/TM data, in Proceedings of the 36th Annual Meeting of the Remote Sensing Society of Japan, (2004), pp.57 - 58. (*in Japanese*)

Yoshii, Y., Kuze, H., Takeuchi, N., Long-path measurement of atmospheric NO_2 with an obstruction flashlight and a charge-coupled-device spectrometer. Appl. Opt., Vol. 42, (2003), pp. 4362-4368, ISSN 0003-6935

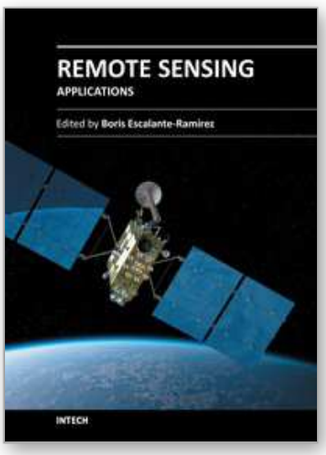

Remote Sensing - Applications
Edited by Dr. Boris Escalante

ISBN 978-953-51-0651-7
Hard cover, 516 pages
Publisher InTech
Published online 13, June, 2012
Published in print edition June, 2012

Nowadays it is hard to find areas of human activity and development that have not profited from or contributed to remote sensing. Natural, physical and social activities find in remote sensing a common ground for interaction and development. This book intends to show the reader how remote sensing impacts other areas of science, technology, and human activity, by displaying a selected number of high quality contributions dealing with different remote sensing applications.

InTech Europe
University Campus STeP Ri
Slavka Krautzeka 83/A
51000 Rijeka, Croatia
Phone: +385 (51) 770 447
Fax: +385 (51) 686 166
www.intechopen.com

InTech China
Unit 405, Office Block, Hotel Equatorial Shanghai
No.65, Yan An Road (West), Shanghai, 200040, China
中国上海市延安西路65号上海国际贵都大饭店办公楼405单元
Phone: +86-21-62489820
Fax: +86-21-62489821

IntechOpen